

## RESEARCH ARTICLE

# Effect of the Mn and Cr contents on the oxidation and creep resistance at 1100°C of cast cantor–based high entropy alloys

P. Berthod<sup>1,2,\*</sup>, L. Aranda<sup>2</sup>, C. Gay<sup>1</sup>, N. Chenikha<sup>1</sup>, P. Spaeter<sup>1</sup>, E. Etienne<sup>2</sup>, G. Medjahdi<sup>2</sup>, A. Vernière<sup>1,2</sup>

<sup>1</sup> Faculty of Sciences and Technologies, University of Lorraine, 54500 Vandoeuvre–lès–Nancy, France

<sup>2</sup> Jean Lamour Institute, University of Lorraine, Nancy, 54000 Nancy, France

Phone: +33(0)372742729; Fax.: +33(0)372742401

**ABSTRACT** - Cast High Entropy Alloys (HEAs) derived from the Cantor's composition may represent alternative substitutional solutions to the superalloys which are constituted for more than half of the critical elements nickel and cobalt. Metallography control (MC)–alloyed HEAs constituted by a Cantor's type matrix associated to an efficient interdendritic network of MC carbides, have demonstrated promising creep resistance at elevated temperatures. Regrettably, they also show poor high temperature oxidation resistance. This bad oxidation behavior is possibly due to the deleterious effect of manganese and to a too low content in chromium. New alloys were elaborated and tested in oxidation at 1100°C with thermogravimetry follow–up and metallographic characterisation, and their creep behavior was controlled. With less Mn and more Cr than the original alloys, these new alloys demonstrated significant progress in oxidation resistance. These changes in chemical compositions did not modify their creep resistances which were globally maintained, for the carbide-free alloy as well as for the MC-containing ones. These Mn-decreased and Cr-increased MC-containing alloys can be considered as low-cost alternative to polycrystalline Ni or Co-based superalloys for working in moderate conditions of corrosive fluids and applied mechanical stresses.

## ARTICLE HISTORY

Received : 13<sup>th</sup> Nov. 2023

Revised : 15<sup>th</sup> Mar. 2024

Accepted : 25<sup>th</sup> Mar. 2024

Published : 26<sup>th</sup> June 2024

## KEYWORDS

CoNiFeMnCr

Manganese

Chromium

TaC and HfC

Hot Oxidation

High temperature creep

## 1. INTRODUCTION

The new century has seen appearing and developing a new metallurgical principle: the High Entropy Alloys (HEAs) and the Medium Entropy Alloys or Multi-principal Element Alloys (MEAs) [1]. Some of them are close to high temperature alloys which combine the classical base elements of superalloys – that is Co, Ni and Fe – for mechanical strength, Al and Cr for corrosion resistance [2]. Some high entropy alloys are even considered as eutectic [3]. One of the most common elements combinations in HEAs is the Co–Ni–Fe–Mn–Cr quinary system [4, 5]. Many of the HEAs which involve these five elements are chosen to be equimolar [6–8].

HEAs and even MEAs are chemically different from superalloys, because of the predominance of one element serving as base of the superalloy whatever its generation [9,10]: the most popular base elements are Ni and Co, sometimes Fe (e.g. ferritic oxide dispersion strengthened superalloys). Nowadays Ni and Co are more and more considered as critical elements, i.e. expensive and subject to possible problems of availability. Their partial replacement by equivalent (but not critical) elements may be usefully considered. This may lead to chemical compositions looking as the HEAs ones. In contrast with the RHEA (refractory high entropy alloys, which involve elements such as Ta, W...), the usual HEAs are generally not designed for applications at high temperature – that is > 1000 °C – for service conditions involving mechanical stresses and oxidation. One can understand why by considering the fast deformation of an equimolar CoNiFeMnCr under a few tens of MPa at 1000 °C. However, strengthening solutions inspired from superalloys can be of interest for improving mechanical resistance at high temperature up to levels starting to be interesting. Among these solutions, carbides – the formation of which is easy to promote in casting process – represent a serious option. This was recently experimented with the successful obtention of cast HEAs based on the equimolar CoNiFeMnCr added with C and Ta or Hf [11]: in both cases an interdendritic population of script–like TaC or HfC eutectic carbides were obtained. The exploration of the high temperature properties showed that these carbides improved outstandingly the creep resistance at 1000 °C and even at 1100 °C [12]. Unfortunately, it was also observed that the CoNiFeMnCr with TaC or HfC were poorly resistant against oxidation, as the base equimolar CoNiFeMnCr alloy [11]. The post-mortem characterization of the oxidized alloys pointed out the responsibility of the too low Cr content (20 wt.%) and of the deleterious role of Mn. The importance of chromium in high temperature oxidation and the threshold to respect in Cr content for several types of superalloys (e.g. Ni–based or Co–based) have been well known for a long time [13, 14]. Concerning manganese, Laplanche et al [15] earlier noted its particular behavior in the oxidation of CrMnFeCoNi high entropy alloy at 700 and 800 °C, and its involvement in the rate–limiting process. The detrimental effect of Mn on high temperature oxidation of Cantor's alloy was also evidenced by Holcomb [16] who proposed to lower its content to improve the oxidation behavior over the [650, 750 °C] range. Li et al [17] attributed the fast oxidation at 900 °C of nanocrystalline CrMnFeCo–Ni thin films to a particularly quick outwards diffusion of manganese. Mahaffey et al. [18], who noted very extended Mn

\*CORRESPONDING AUTHOR | P. Berthod | ✉ [patrice.berthod@univ-lorraine.fr](mailto:patrice.berthod@univ-lorraine.fr)

depletion, pointed out the vapor pressure of Mn which is high compared to the other elements of the Cantor's alloy. The detrimental effect of Mn was also recently observed by Bürckner et al. [19] who substituted Mn by Cu and/or Al at 600 °C and 800 °C and observed significant improvement in oxidation resistance.

To solving this problem of bad oxidation behavior, it was intended in this work to replace a half part of the unfavorable element Mn by the equivalent quantity of the favorable element Cr. The resulting alloys were tested in oxidation at 1100 °C, a temperature much higher than the ones of the earlier oxidation tests applied to this kind of alloy. The aim is here to study the evolution, from the equimolar versions of these alloys, of the oxidation resistance. In parallel, a control of the creep resistance at the same temperature was carried out for these new TaC- or HfC-reinforced HEAs.

## 2. MATERIALS AND METHODS

Three novel alloy compositions were considered to possibly improve the high temperature oxidation behavior for alloys derived from the equimolar (Cantor's) composition. They are CoNiFeMn<sub>0.5</sub>Cr<sub>1.5</sub> without or with the introduction of either C and Ta, or C and Hf, in quantities chosen to finally achieve 0.25 wt. % C and 3.7 wt. % Ta (or 3.7 wt. % Hf). By comparison to the Cantor composition, the Mn content is divided by 2 while the Cr content is multiplied by 1.5. These alloys are thus more MEAs than really HEAs. They were elaborated using high frequency induction to melt together pure individual elements under inert atmosphere. Prior to cutting, the obtained ingots – characterized by an ovoid shape and a weight of about 40 g – were embedded in resin to facilitate handling during machining. Using a metallographic saw, one obtained part for metallography control (MC), {2 mm × 2 mm × 8 mm} samples for the Differential Thermal Analysis (DTA), {2 mm × 8 mm × 8 mm} samples for the Thermogravimetry Analysis (TGA) and {17 mm × 2 mm × 1.5 mm} samples for the 3-Points Flexural Creep tests (3PFC). Except the samples for DTA, all dimensions were carefully measured for the accurate calculation of the surfaces (TGA) and of the central load to apply for achieving the targeted stress. Except the ones for DTA, the surfaces of the samples were prepared with #1200-grit papers, with smoothing of the edges and corners of the TGA samples (to avoid local over-oxidation). Concerning the MC samples, after new embedding, they were ground with SiC papers under water, the granulometry of which varying from #240 to #1200. They were then polished with textile disk enriched with 1 µm alumina hard particles.

The DTA experiments were carried out using a SETARAM TG-ATD 92-16.18 apparatus. The sample was heated up to 1100 °C at 20 K min<sup>-1</sup>, then to 1450 °C at 5 K min<sup>-1</sup>. It was thereafter cooled at -5 K min<sup>-1</sup> down to 1100 °C, then to room temperature at -20 K min<sup>-1</sup>. The low heating and cooling rates between 1100 °C and 1450 °C allowed accurate determination of the temperatures of start and end of fusion and solidification. The 3PFC experiments used a SETARAM TMA 92-16.18 thermodilatometer modified to allow performing 3-points bending creep tests. The upper point was the alumina stem connected to a displacement sensor, and the two bottom points were alumina rods. The load, rated to induce the targeted maximal stress of 20 MPa, was calculated as a function of the thickness and width of the sample. The thermal cycle was heating (and cooling) up to (and from) 1100 °C (temperature of the 150 h-isothermal stage) with the +/-20K min<sup>-1</sup> rate. The TGA experiments were carried out with a SETARAM TG92-16.16 thermo-balance. The tests were performed in a flow of 2 L h<sup>-1</sup> of dry synthetic air. The followed thermal cycle was heating at +20 K min<sup>-1</sup> up to 1100 °C, isothermal stage for 50h at 1100 °C, and cooling at -5 K min<sup>-1</sup>.

X-ray diffraction (XRD) was performed on the oxidized surfaces. The diffractometer was a D8 Advance model from Brüker, and this is the Copper K $\alpha$  radiation ( $\lambda = 1.5406$  Angström) which was applied. The obtained diffractograms were exploited using the DIFFRAC.EVA software (Brüker). After XRD, the samples were embedded in resin to prevent any deterioration of the external oxides scales during the cutting performed for obtaining two cross-sectional samples. These cross-sectional samples were ground and polished similarly to the MC samples above. A Scanning Electron Microscope (SEM) with an Energy Dispersive Spectrometer (EDS) was used to control the microstructures and the chemical compositions of the MC samples. This SEM (JEOL JSM 6010-LA), working with an acceleration voltage of 15 or 20 kV, mainly in Back Scattered Electrons mode (BSE), were also used to characterize the cross-sectional samples (external oxide scales, internal oxides, general subsurface degradation due to oxidation).

## 3. RESULTS AND DISCUSSION

### 3.1 Characteristics of the Alloys

The compositions of the obtained alloys are given in Table 1. The as-cast microstructures observed with the SEM are illustrated in Figure 1. The targeted contents in all elements were all obtained. In the case of carbon, EDS is not suitable to measure its content. However, considering that the carbon is systematically respected for the same elaboration protocol as earlier regularly checked by spark spectrometry and also that the carbide population is typical of 0.25 wt.% C containing alloys, it is assumed here that the MEA/TaC and MEA/HfC alloys contain carbon with contents very close to 0.25 wt.%. Concerning Ta and Hf, as systematically encountered with EDS measurements, their contents are a little higher than targeted. This overestimation is usual for alloys in which an element is much more present as carbides than in matrix: much harder and wear-resistant than matrix, the TaC and HfC carbides emerge a little out the planar mirror-like surface. They are consequently more exposed to the electron beam. This leads to a little higher response in term of photons arriving to the EDS detector. The Ta and Hf contents have thus to be considered as being well respected too.

The as-cast microstructure developed as solidification cells for the MEA alloy. For the MEA/TaC alloy and the MEA/HfC alloy, solidification started by the development of matrix dendrites of matrix, followed by the interdendritic precipitation of script-like shaped TaC or HfC eutectic carbides. In addition, for the MEA/HfC alloy, one must mention the inhomogeneous presence of rare blocky HfC which are possibly pre-eutectic carbides, crystallized prior to dendritic development. These microstructures in the as-cast state are similar to the ones previously obtained for the equimolar versions of these alloys [11]. Obviously, the decrease in Mn and the increase in Cr did not influence the as-cast microstructures of these alloys: (a) the matrix is still dendritic which is of importance for the mechanical properties at high temperature, (b) the TaC and HfC carbides are of a eutectic nature (and the new alloys should take benefit again from their script-like shape in the mechanical field at high temperature), (c) no additional chromium carbides are present in addition to the TaC or HfC carbides and thus no decrease in melting point is expected. This is a first important result.

Table 1. Controlled chemical compositions of the three alloys (from five  $\times 250$  full frame EDS analyses per alloy); weight contents in all elements except carbon (for C: 0.25 wt.% for the MEA/TaC and MEA/HfC alloys)

Alloy	Average/Std dev.	Co	Ni	Fe	Mn	Cr	Ta or Hf
MEA	Average	20.0	20.5	19.8	8.3	31.3	/
	Std dev.	0.1	0.3	0.2	0.5	0.4	
MEA/TaC	Average	19.5	20.0	19.1	8.4	28.5	4.6
	Std dev.	0.2	0.5	0.3	0.2	0.3	0.2
MEA/HfC	Average	19.7	20.1	19.1	8.8	27.8	4.5
	Std dev.	0.4	0.3	0.3	0.3	0.7	0.6

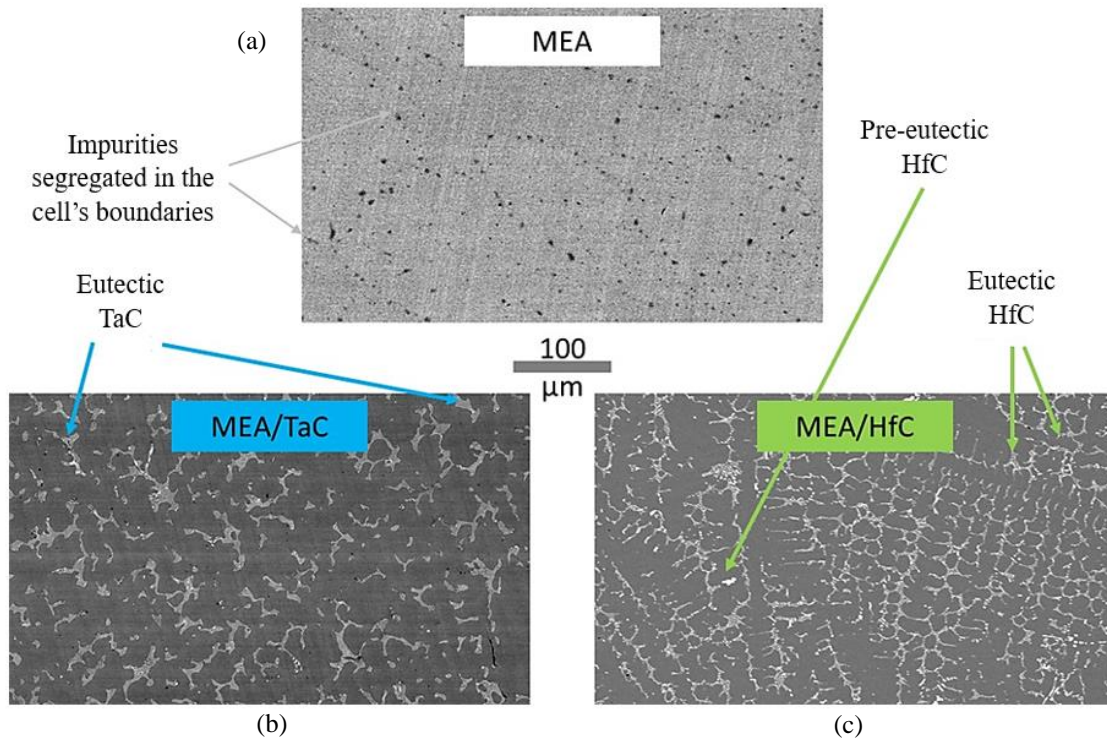


Figure 1. As-cast microstructures of the three alloys MEA: (a)  $\text{CoNiFeMn}_{0.5}\text{Cr}_{1.5}$ , (b) MEA/TaC: MEA + 0.25C + 3.7Ta (wt.%) and (c) MEA/HfC: MEA + 0.25C + 3.7Hf (wt.%)

### 3.2 Differential Thermal Analysis

The obtained DTA curves are drawn in Figure 2, with on the left the same range heat flow values for the three alloys for easy comparison, and on the right ranges allowing better visualization of the start and end of the thermal exchange phenomena. Their exploitation led to the temperature values of start and end for both melting and solidification, written in Table 2. The MEA presents a broad single endothermic peak at heating (melting of the matrix which is the single phase) and a single exothermic peak (started abruptly because of undercooling and instantaneous nucleation) at cooling. There are two more or less extended peaks at heating and at cooling for the MEA/TaC alloy: the two low temperature ones for the {matrix, TaC} eutectic and the two high temperature ones for the pre-eutectic dendrites of matrix. For the MEA/HfC alloy, by comparison to the MEA/TaC one, a third high temperature small peak for the heating and for the cooling is noticed. It is due to the melting and the re-crystallization of the pre-eutectic HfC.

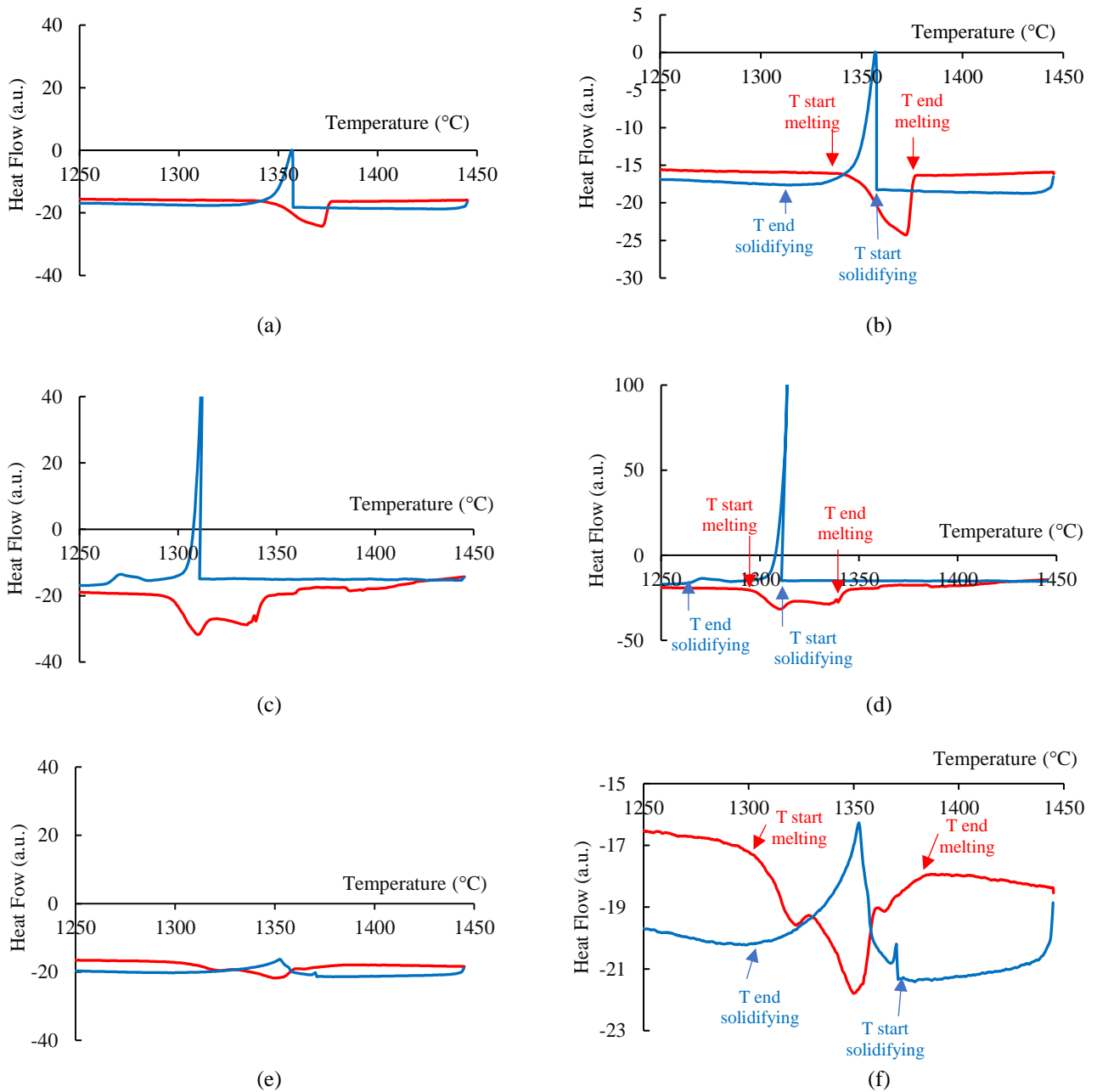


Figure 2. The DTA curves plotted versus temperature: (a-b) MEA alloy, (c-d) MEA/TaC alloy, (e-f) MEA/HfC alloy. (a, c, e) is same range for all alloys and (b, d, f) is automatic range for each alloy

Table 2. Values of the temperature of melting and solidification beginnings and ends, and of the liquidus and solidus temperatures which can be estimated with these results

Alloy	Melting (°C)		Solidification (°C)		Average (°C)	
	Start	End	Start	End	Solidus	Liquidus
MEA	1338	1377	1358	1316	1327	1358
MEA/TaC	1289	1351	1314	1259	1274	1333
MEA/HfC	1289	1395	1388	1290	1290	1392

The temperatures of melting start and the liquidus temperatures are high for the MEA alloy (around 1330 °C), and 40 °C lower for the two carbide-containing alloys (1290 °C). This difference is to be attributed to the presence of eutectic carbides in the MEA/TaC and MEA/HfC alloys which were the last compounds to crystallize at solidification and which constitute the alloy regions that are the first to melt when the alloy is reheated. Obviously, these three {modified Cantor}-based alloys, the MEA alloy but also the MEA/TaC and MEA/HfC alloys despite their lower melting start temperatures, are all refractory enough to allow testing them at 1100 °C in oxidation and in creep, as this was previously the case for their equimolar versions.

### 3.3 Creep Resistance Control

Prior to the oxidation tests, the creep tests were performed to initially check whether the good properties of the TaC–reinforced and HfC–reinforced Cantor alloys are not deteriorated because of the change of the matrix from HEA (equimolar) to MEA (not equimolar), since the Mn decrease, and the Cr increase may have consequences on the high temperature mechanical properties. Considering the comments written above concerning the apparent absence of any change in the as–cast microstructure between the new alloys and their initial versions, the creep performances are expected to be the same, but this needs to be confirmed. The obtained deformation curves and the deformation rate variation versus time are plotted in Figure 3 and quantitatively exploited in Table 3. They first confirm, for these new alloys, that the very beneficial effect of the presence of the TaC or HfC carbides, earlier observed for the equimolar versions [9], also exist for these new versions with modified Mn and Cr contents. Indeed, these new results allow evidencing that the two TaC– or HfC–containing alloys are much more creep–resistant than the carbide–free modified Cantor’s alloy (which deformed as rapidly as the equimolar Cantor’s alloy [12] in the same conditions of stress and temperature). Indeed, there are two orders of magnitude between the steady state or linear deformation rate between the {TaC or HfC}–containing alloys and the carbide–free alloy (the tertiary creep regime of which came very early). The values of linear deformation rate are rather close to the ones earlier obtained for the equimolar versions [12].

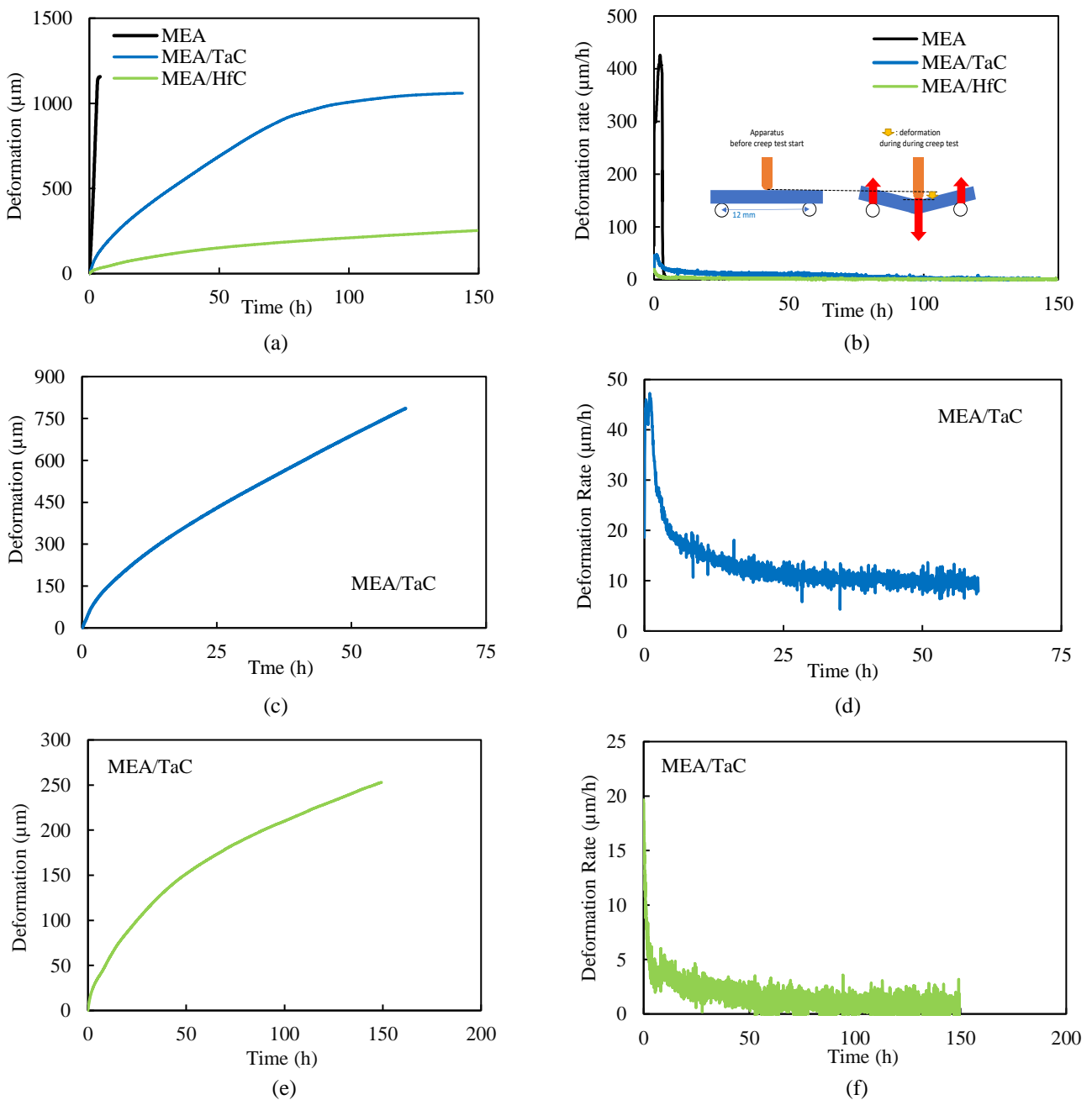


Figure 3. The 3PFC curves of alloys under 20 MPa at 1100°C: (a) deformation of the MEA alloy versus time, (b) corresponding deformation rate versus time with insertion of a scheme of the 3PFC test, (c-d) the individual curves for the MEA/TaC alloy; (e-f) the individual curves for the MEA/HfC alloy

The TaC or HfC script-like carbides present in the interdendritic spaces of the equimolar alloys cast alloys which strengthened outstandingly the initial equimolar versions [12] play thus again this role for these present Mn-impoverished and Cr-enriched versions. One can remind that these carbides, due to their particular morphologies inherited from their eutectic origin, consolidate together neighbor dendrites. Despite of the accumulation of the sliding steps resulting from the continual arrival of dislocations during the steady stage of creep, the increasing cavitation did not succeed in producing interdendritic decohesion and the transition from the second (steady stage) to the third stage of creep is considerably delayed by comparison to what occurs for the simple Cantor's alloy. This is the same effect of the TaC and HfC carbides that one observes here for the present Mn-impoverished and Cr-enriched versions.

Table 3. Values of some parameters characterizing the creep behaviors of the three alloys

Alloy	Stage I		Stage II		Stage III
	Duration	Deformation	Duration	Deform. rate	Duration
MEA	≈ 0.2h	44 μm	≈ 0.5h	300 μm/h	> 2.5h
MEA/TaC	≈ 20h	370 μm	> 50h	10 μm/h	Not reached
MEA/HfC	≈ 70h	170 μm	> 150h	0.8 μm/h	Not reached

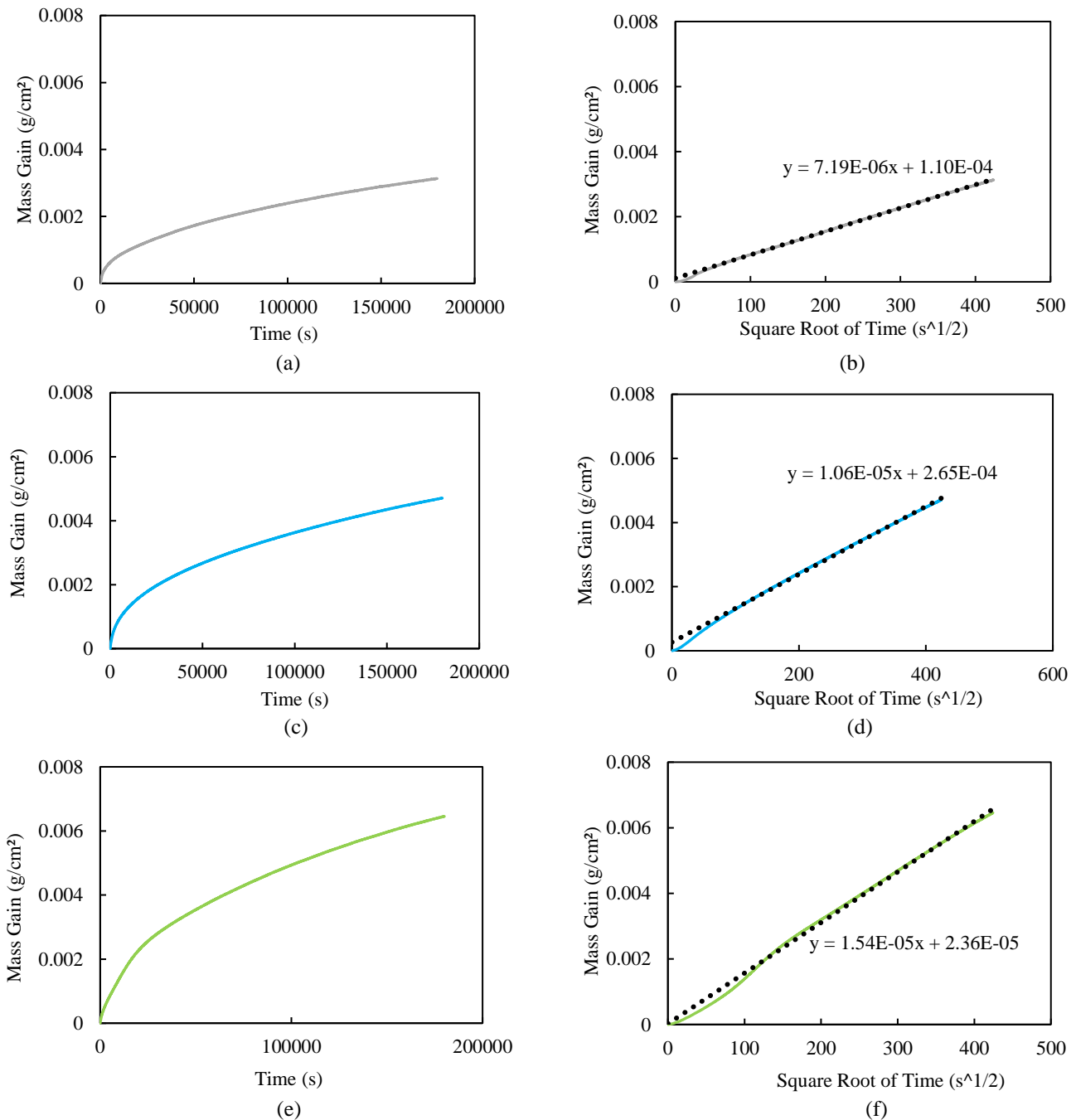


Figure 4. The TGA curves oxidized for 50h at 1100°C: (a-b) MEA alloy; (c-d) MEA/TaC alloy and (e-f) MEA/HfC alloy

### 3.4 Thermogravimetry Characterization of High Temperature Oxidation

The three obtained mass gain curves, plotted first versus time and second versus the square root of time, are given in Figure 4. The shape of the three curves plotted versus time is obviously parabolic, and they can be hierarchized as follows: MEA < MEA/TaC < MEA/HfC according to the mass gain order. The curves plotted versus the square root of time become rather linear and the slope of these straight lines can be converted in values of the oxidation parabolic constant (denote as  $K_p$ ), according to the following calculation:  $K_p = 0.5 \times \text{slope}^2$ . The values displayed in Table 4 are several times lower than the ones assessed for the equimolar versions of these alloys at the same temperature (e.g.  $28 \times 10^{-12} \text{ g}^2 \text{ cm}^{-4} \text{ s}^{-1}$  for the MEA alloy against  $160 \times 10^{-12} \text{ g}^2 \text{ cm}^{-4} \text{ s}^{-1}$  for the equimolar Cantor alloy [20]). Despite that they are also slightly higher than the chromia-forming Ni-30wt.%Cr alloy ( $K_p \approx 20 \times 10^{-12} \text{ g}^2 \text{ cm}^{-4} \text{ s}^{-1}$  [21]), the improvement is significant. Oxidation is well slowed down due to the Cr content increase associated to the Mn content decrease. Metallographic investigations were carried out on the oxidized samples to understand how these changes in Mn and Cr contents succeeded in decreasing the oxidation rate.

Table 4. Values of the parabolic constants characterizing the oxidation kinetics of the three alloys

$K_p$	MEA alloy	MEA/TaC alloy	MEA/HfC alloy
	$28 \times 10^{-12} \text{ g}^2 \text{ cm}^{-4} \text{ s}^{-1}$	$65 \times 10^{-12} \text{ g}^2 \text{ cm}^{-4} \text{ s}^{-1}$	$120 \times 10^{-12} \text{ g}^2 \text{ cm}^{-4} \text{ s}^{-1}$

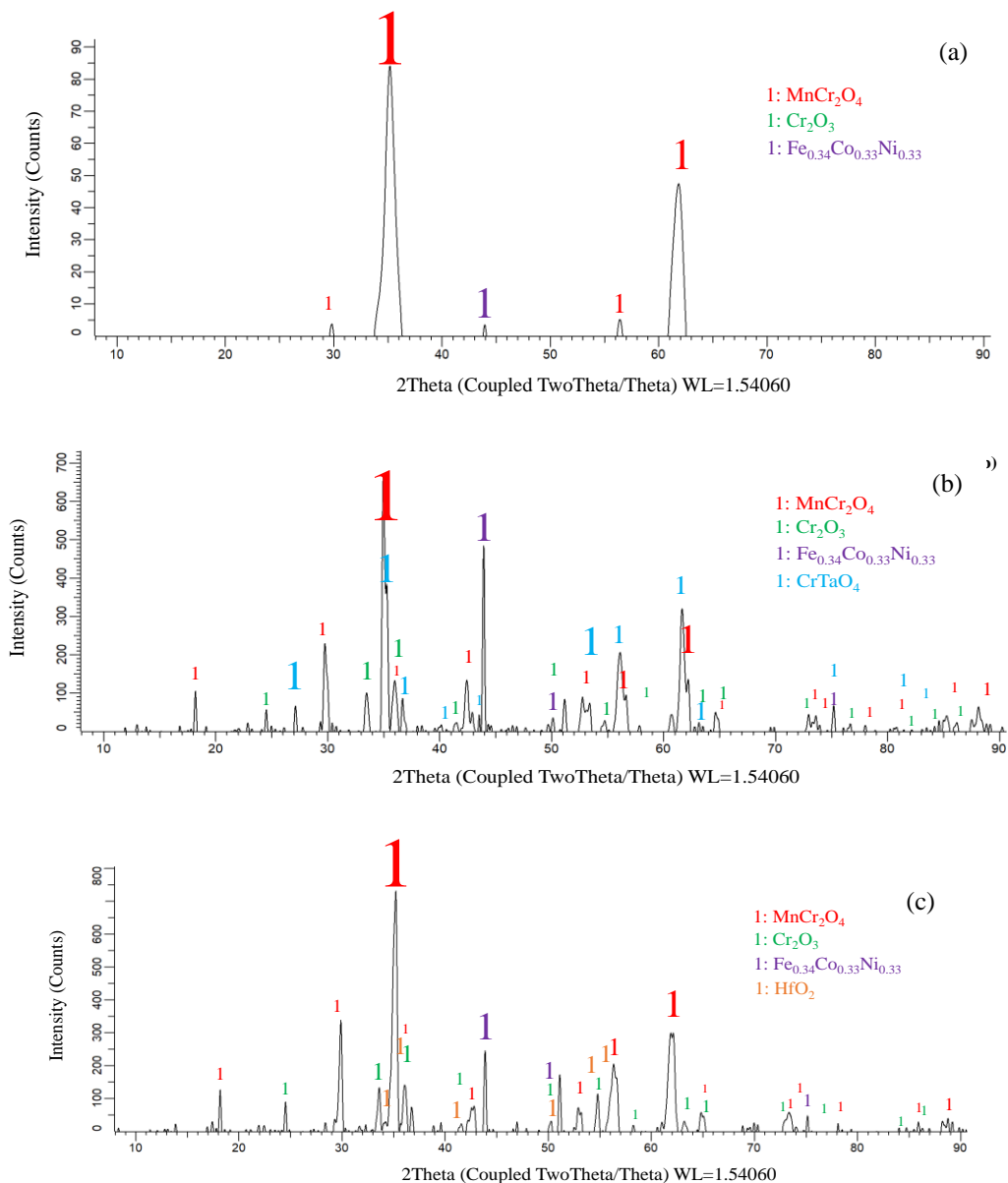


Figure 5. The diffractograms obtained on the oxidized surfaces of the samples after the TGA tests: (a) MEA alloy; (b) MEA/TaC alloy and (c) MEA/HfC alloy

### 3.5 Post-mortem Characterization of High Temperature Oxidation

The oxidized samples were first subjected to XRD. The obtained diffractograms are given in Figure 5. Seemingly, two oxides are common to the three alloys:  $\text{MnCr}_2\text{O}_4$  (spinel oxide) and  $\text{Cr}_2\text{O}_3$ . One notes also the presence of  $\text{CrTaO}_4$  for the MEA/TaC and  $\text{HfO}_2$  MEA/HfC. Concerning the natures of the oxides which formed, the main difference with the equimolar versions oxidized also for 50 hours at 1100 °C is: here the main oxide is the  $\text{MnCr}_2\text{O}_4$  spinel while this was apparently a  $\text{Mn}_3\text{O}_4$  oxide for the equimolar versions [20]. This difference of main oxide is easily understandable when one takes into account the differences in Mn and Cr contents in the two kinds of alloys: less Mn and more Cr logically favors the formation of oxides richer in Cr and poorer in Mn, that is  $\text{MnCr}_2\text{O}_4$  at the expense of  $\text{Mn}_3\text{O}_4$ . Since the diffusion of the ionic species involved in the oxidation phenomenon is usually less easy in spinels than in non-stoichiometric oxides, this can be a first explanation of the lower oxidation kinetics of the present Mn-impooverished Cr-enriched alloys. Cross-sectional views of the oxidized surfaces and subsurface are presented in Figure 6. The external scales are still not present everywhere, notably for the MEA/TaC alloy for which it was difficult to find areas where the external scale was still here. Obviously, spallation at cooling was important, especially for the MEA/TaC alloy. The scales are composed of superposed oxide parts, one outer containing Mn in addition to chromium, and another inner part much richer in chromium. Internal oxidation occurred for the MEA/TaC alloy: TaC dissolution, Ta diffusion towards the oxidation front, and  $\text{CrTaO}_4$  formation in subsurface. In the case of the MEA/HfC alloy, hafnium oxide formed in situ by progressive conversion of HfC carbide into  $\text{HfO}_2$  oxide. The elemental distribution of oxygen and of the different metals, after oxidation, is illustrated in Figure 7 for the MEA alloy, in Figure 8 for the MEA/TaC alloy, and in Figure 9 for the MEA/HfC alloy. They illustrate the comments written above about the oxide scales and the internal oxidation.

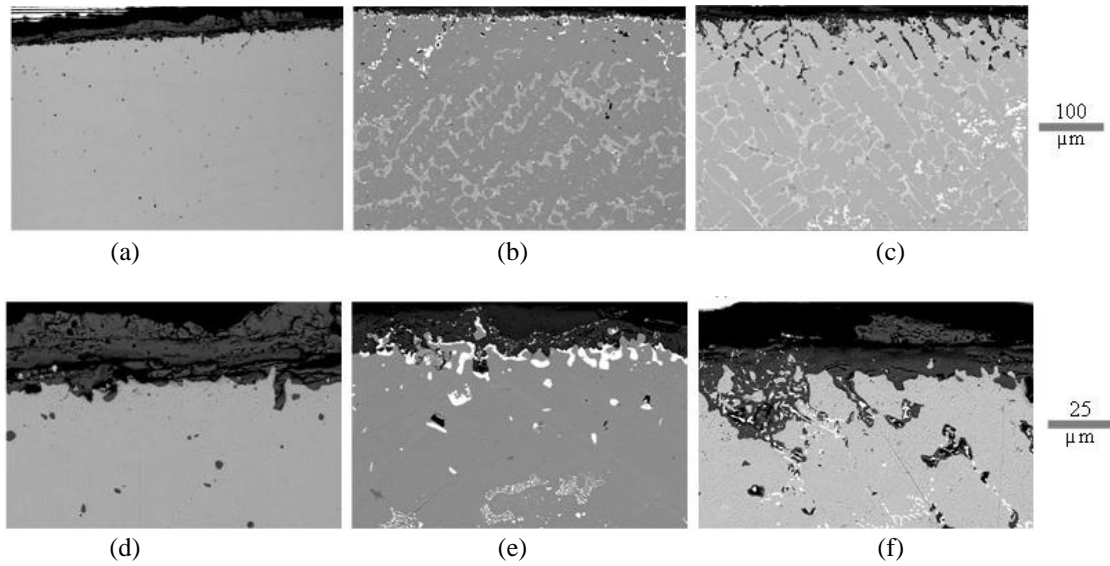


Figure 6. SEM/BSE micrographs of oxidized surfaces: (a) MEA at low magnification, (b) MEA/TaC at low magnification, (c) MEA/HfC at low magnification, (d) MEA at high magnification, (e) MEA/TaC at high magnification and (f) MEA/HfC at high magnification.

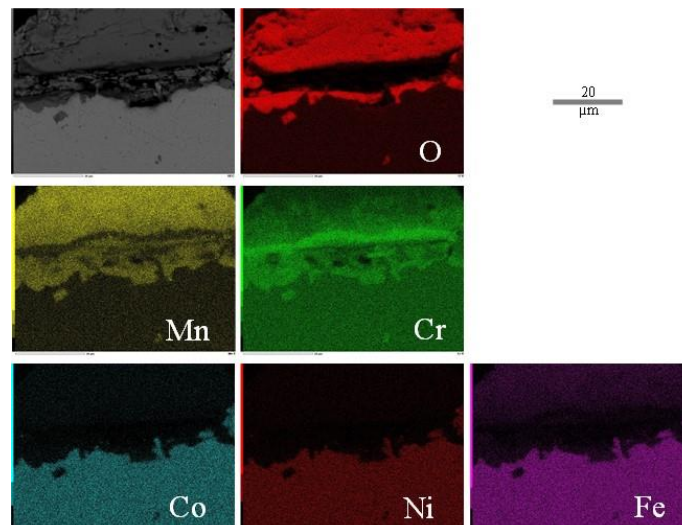


Figure 7. Elemental distribution in the oxidized surface and subsurface of the MEA alloy (EDS X-maps)

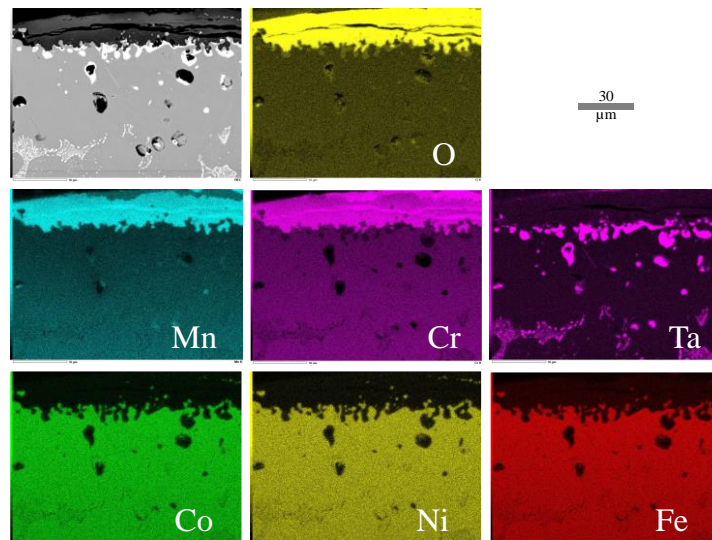


Figure 8. Elemental distribution in the oxidized surface and subsurface of the MEA/TaC alloy (EDS X–maps)

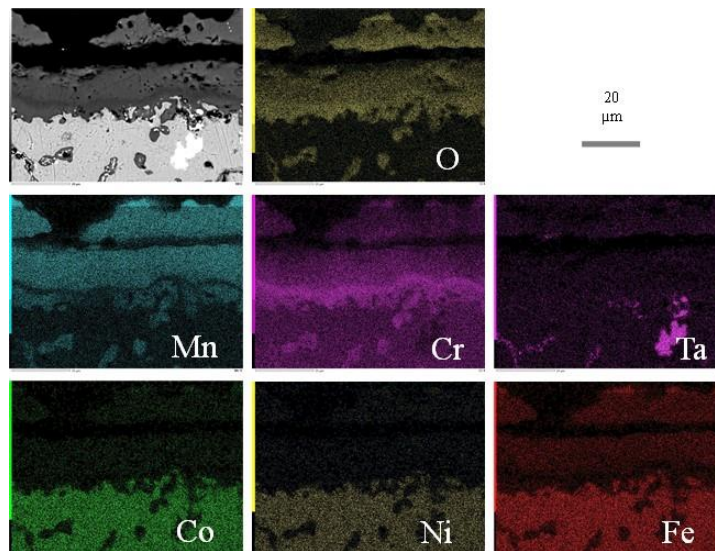


Figure 9. Elemental distribution in the oxidized surface and subsurface of the MEA/HfC alloy (EDS X–maps)

Despite the loss of a part of the external oxide scale by spallation during cooling, it appears thus that the alloys were really covered by superposed oxide scales all along the sample surfaces exposed to oxidation. Among these superposed scales there was one made of  $\text{MnCr}_2\text{O}_4$ , richer in Cr and poorer in Mn than what was observed on the surface of the equimolar versions after oxidation [20]. This can explain the slower oxidation kinetics observed for the present alloys. To know more quantitatively the chemical evolution in subsurface, EDS profiles were acquired inwards, from the interface separating the oxide scale and the alloy, perpendicularly to this interface (Figure 10). The minimal Cr and Mn contents close to the scale/alloy interface and the corresponding depleted depths, measured on several profiles per alloy, are given in Table 5. The obtained profiles evidence the impoverishments in Cr over a 100–130  $\mu\text{m}$  depth and of Mn over 110–180  $\mu\text{m}$ . For Cr, these values are similar to what was observed for the equimolar versions but, concerning Mn, they are lower than for the equimolar versions (100–140  $\mu\text{m}$  for Cr and 140–250  $\mu\text{m}$  for Mn [20]). Close to the oxidation front, the Cr content has significantly decreased (10 wt.%Cr less, as for the equimolar versions), and much more for Mn (4 wt.% Mn less, against 8 wt.% Mn less for the equimolar versions). This indicates that the Cr quantity per surface unit area which left the present alloys to be oxidized is globally the same as for their equimolar versions previously oxidized in the same conditions [20] while the Mn quantity lost by the present alloys is significantly lower than for the equimolar versions. This is consistent with the lower  $K_p$  obtained here and for the differences of nature of the main oxide ( $\text{MnCr}_2\text{O}_4$  spinel here against  $\text{Mn}_3\text{O}_4$  for the equimolar versions). Concerning the distribution of tantalum in the subsurface of the oxidized MEA/TaC alloy, one can notice that the Ta content is lowered close to the oxidation front by comparison with the about 1.5 wt.%Ta initially present in the matrix. In contrast, hafnium, which was initially inexistent in the matrix of the MEA/HfC, is, after oxidation test, still totally absent in the matrix, in the subsurface as well as in the bulk. Contrarily to Ta which was in equilibrium between the carbide phase and the matrix in the bulk of the as-cast MEA/TaC alloy as well as after aging, Hf is still wholly involved in carbides in the bulk of the MEA/HfC alloy, and in internal oxides formed in the subsurface after oxidation.

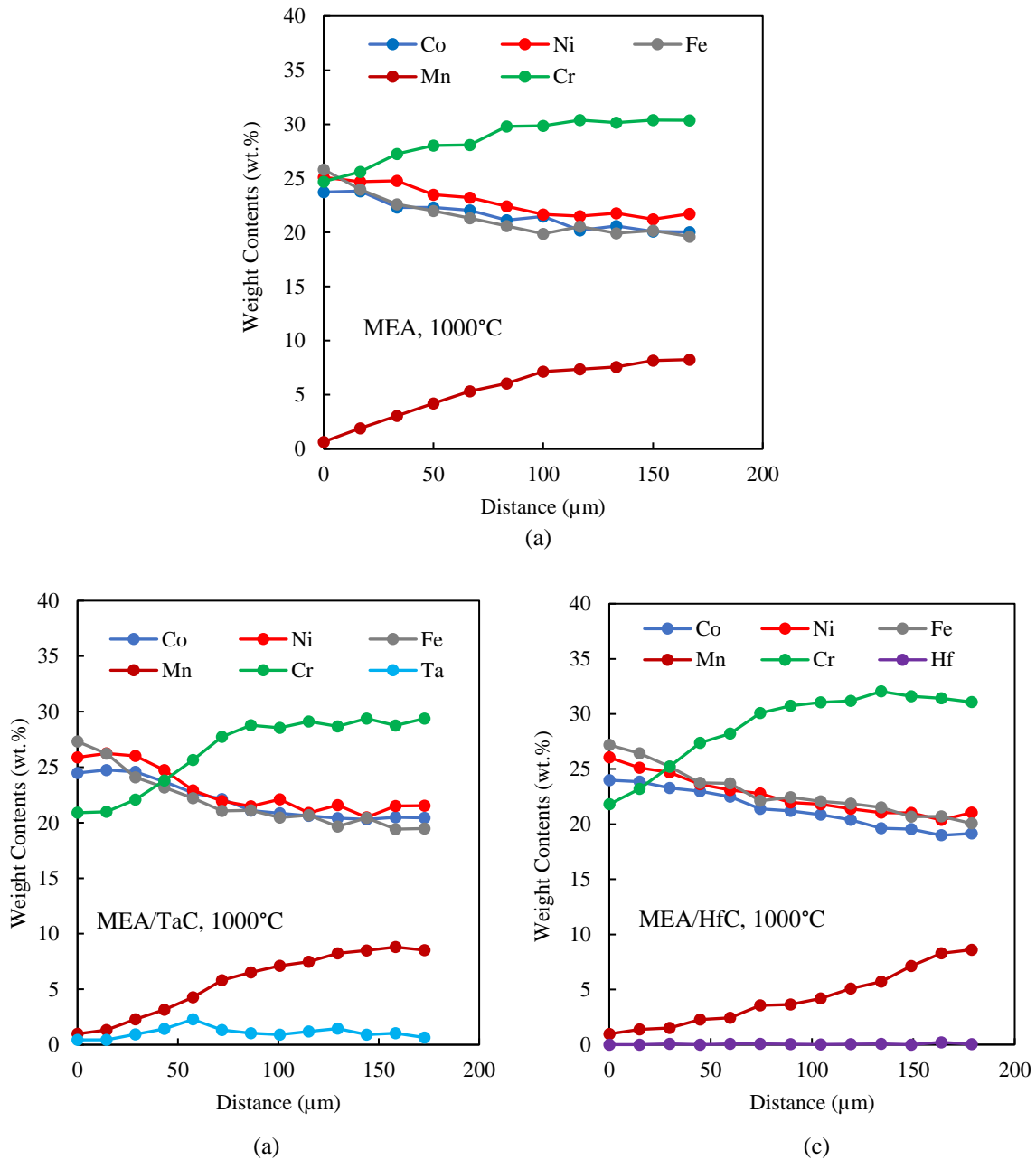


Figure 10. EDS concentration profiles acquired across the part of subsurface affected by oxidation of: (a) MEA alloy, (b) MEA/TaC alloy and (c) MEA/HfC alloy

Table 5. Distribution characteristics of Cr and Mn deduced from the exploitation of the EDS profiles

Alloy		Cr mini (wt.%)	Cr-depleted depth (μm)	Mn mini (wt.%)	Mn-depleted depth (μm)
MEA alloy	Max	25.5	131	1.7	150
	min	23.4	96	0.5	115
MEA/TaC	Max	21.1	115	1.0	158
	min	20.7	86	0.7	144
MEA/HfC	Max	21.8	134	1.0	179
	min	20.7	96	0.8	144

#### 4. CONCLUSIONS

A remarkable improvement of the oxidation behavior at 1100 °C by decreasing the Mn content and increasing the Cr one in these Cantor-based alloys alloyed or not with TaC or MC carbides was successfully obtained as expected. In addition, this higher oxidation resistance was fortunately not accompanied neither by microstructure modification nor by the loss of the interesting creep resistance provided by the TaC or HfC eutectic carbides. The two MC-strengthened alloys

stay hugely superior to the quinary alloy with deformation rate of only  $1 - 10 \mu\text{m h}^{-1}$  against  $300 \mu\text{m h}^{-1}$  for the MEA alloy. However, the  $K_p$  values of  $3, 7$  and  $12 \times 10^{-11} \text{ g}^2 \text{ cm}^{-4} \text{ s}^{-1}$  for the MEA, MEA/TaC and MEA/HfC alloys, remain higher than the ones of chromia-forming alloys (e.g.  $\approx 2 \times 10^{-11} \text{ g}^2 \text{ cm}^{-4} \text{ s}^{-1}$  for Ni-30wt.%Cr), because of the different but still perfectible external oxide scale, and also of the behavior of Mn. The manganese involvement in oxidation is still of similar importance as chromium, despite its content in alloy being three times lower.

## ACKNOWLEDGMENTS

The authors would like to acknowledge the X-Gamma service of the Institute Jean Lamour for the access to the diffractometer. This study was not supported by any grants from funding bodies in the public, private, or not-for-profit sectors.

## CONFLICT OF INTEREST

The authors declare no conflicts of interest.

## AUTHORS CONTRIBUTION

P. Berthod (Conceptualization; Formal analysis; Visualisation; Supervision; Methodology; Data curation; Writing – original draft)

L. Aranda (Data curation; Resources)

C. Gay, N. Chenikha (Formal analysis)

E. Etienne, G. Medjahdi, A. Vernière (Resources)

## REFERENCES

- [1] P. Wilson, R. Field, M. Kaufman, "The use of diffusion multiples to examine the compositional dependence of phase stability and hardness of the Co-Cr-Fe-Mn-Ni high entropy alloy system," *Intermetallics*, vol. 75, pp. 15–24, 2016.
- [2] J. Dabrowa, W. Kuczka, G. Cieslak, T. Kulik, M. Danielewski, J.-W. Yeh, "Interdiffusion in the FCC-structured Al-Co-Cr-Fe-Ni high entropy alloys: Experimental studies and numerical simulations," *Journal of Alloys and Compounds*, vol. 674, pp. 465–462, 2016.
- [3] A. Shafiei, "The design of eutectic high entropy alloys in Al-Co-Cr-Fe-Ni system," *Metals and Materials International*, vol. 27, pp. 127–138, 2021.
- [4] G. Bracq, M. Laurent-Brocq, L. Perrière, R. Pirès, J.-M. Joubert, I. Guillot, "The fcc solid solution stability in the Co-Cr-Fe-Mn-Ni multi-component system," *Acta Materialia*, vol. 128, pp. 327–336, 2017.
- [5] C. Konkati, A. Chauhan, "Incipient plasticity of a non-equiatom Co<sub>21.5</sub>Cr<sub>21.5</sub>Fe<sub>21.5</sub>Mn<sub>21.5</sub>Ni<sub>14</sub> multi-principal element alloy", *Metallurgical and Materials Transactions A*, vol. 54, no. 10, pp. 3973–3987, 2023.
- [6] S. H. Joo, H. Kato, M. J. Jang, J. Moon, C.W. Tsai, J.W. Yeh, et al., "Tensile deformation behavior and deformation twinning of an equimolar CoCrFeMnNi high-entropy alloy," *Materials Science & Engineering A*, vol. 689, pp. 122–133, 2017.
- [7] T. Teramoto, K. Yamada, R. Ito, and K. Tanaka, "Monocrystalline elastic constants and their temperature dependences for equi-atomic Cr-Mn-Fe-Co-Ni high-entropy alloy with the face-centered cubic structure," *Journal of Alloys and Compounds*, vol. 777, pp. 1313–1318, 2019.
- [8] M. A. Gianelle, C. Clapp, A. Kundu, and H.M. Chan, "Solid state processing of the cantor derived alloy CoCrFeMnNi by oxide reduction," *Results in Materials*, vol. 14, p. 100286, 2022.
- [9] C. T. Sims, W. C. Hagel. *The Superalloys*, 1st Ed. New York, USA: John Wiley and Sons, 1972.
- [10] M. S. Donachie, S. J. Donachie. *Superalloys: A Technical Guide*, 2nd Ed. USA: ASM International, 2002.
- [11] P. Berthod, "Behavior in oxidation at 1000 °C of carbon-containing equimolar CoNiFeMnCr alloys added with hafnium or tantalum with high contents," *Journal of Chemical Engineering Research Updates*, vol. 9, pp. 60–71, 2022.
- [12] P. Berthod, "Strengthening against creep at elevated temperature of HEA alloys of the CoNiFeMnCr type using MC-carbides," in *Supplemental Proceedings of the TMS 2023 Annual Meeting & Exhibition*, pp. 19–23, 2023.
- [13] P. Kofstad. *High Temperature Corrosion*, 2nd Ed. London, UK: Elsevier Applied Science, 1988.
- [14] D. J. Young. *High Temperature Oxidation and Corrosion of Metals*. 2nd Ed. Amsterdam, Netherlands: Elsevier Corrosion Series, 2016.
- [15] G. Laplanche, U. F. Volkert, G. Eggeler, E. P. George, "Oxidation behavior of the CrMnFeCoNi high-entropy alloy," *Oxidation of Metals*, vol. 85, no. 5-6, pp. 629–645, 2016.

- [16] G. R. Holcomb, J. Tylczak, C. Carney, "Oxidation of CoCrFeMnNi high entropy alloys," *JOM*, vol. 67, no. 10, pp. 2326–2339, 2015.
- [17] Y. J. Li, A. Kostka, A. Savan, A. Ludwig "A. Atomic-scale investigation of fast oxidation kinetics of nanocrystalline CrMnFe-CoNi thin films," *Journal of Alloys and Compounds*, vol. 766, pp. 1080-1085, 2018.
- [18] J. Mahaffey, A. Vackel, S. Whetten, M. Melia, A. B. Kustas, "Structure evolution and corrosion performance of CoCrFeMnNi high entropy alloy coatings produced via plasma spray and cold spray," *Journal of Thermal Spray Technology*, vol. 31, no. 4, pp. 1143–1154, 2022.
- [19] M. L. Bürkner, L. Mengis, E. M. H. White, M. C. Galetz, "Influence of copper and aluminum substitution on high-temperature oxidation of the FeCoCrNiMn "Cantor" alloy," *Materials and Corrosion*, vol. 74, no. 1, pp. 79–90, 2023.
- [20] P. Berthod, "Behaviors in oxidation at 1100 °C of an equimolar CoNiFeMnCr high entropy alloy and of its versions moderately added with HfC or TaC carbides," *High Temperature Corrosion of Materials*, vol. 100, no. 3-4, pp. 177–191, 2023.
- [21] P. Berthod, "Kinetics of high temperature oxidation and chromia volatilization for a binary Ni–Cr alloy," *Oxidation of Metals*, vol. 64, no. 3-4, pp. 235–252, 2005.